Research Article | Vol. 26, No. 11 | 28 May 2018 | OPTICS EXPRESS 14810
Optics EXPRESS

Thin film lithium niobate electro-optic modulator with terahertz operating bandwidth

ANDREW J. MERCANTE,[1,*] SHOUYUAN SHI,[1] PENG YAO,[2] LINLI XIE,[3] ROBERT M. WEIKLE,[3] AND DENNIS W. PRATHER[1]

[1]*Electrical and Computer Engineering Department, University of Delaware, Newark, DE 19716, USA*
[2]*Phase Sensitive Innovations, Inc., 51 East Main Street, Newark, DE 19711, USA*
[3]*Department of Electrical and Computer Engineering, University of Virginia, Charlottesville, VA 22903 USA*
[*]*ajmerc@udel.edu*

Abstract: We present a thin film crystal ion sliced (CIS) $LiNbO_3$ phase modulator that demonstrates an unprecedented measured electro-optic (EO) response up to 500 GHz. Shallow rib waveguides are utilized for guiding a single transverse electric (TE) optical mode, and Au coplanar waveguides (CPWs) support the modulating radio frequency (RF) mode. Precise index matching between the co-propagating RF and optical modes is responsible for the device's broadband response, which is estimated to extend even beyond 500 GHz. Matching the velocities of these co-propagating RF and optical modes is realized by cladding the modulator's interaction region in a thin UV15 polymer layer, which increases the RF modal index. The fabricated modulator possesses a tightly confined optical mode, which lends itself to a strong interaction between the modulating RF field and the guided optical carrier; resulting in a measured DC half-wave voltage of 3.8 $V \cdot cm^{-1}$. The design, fabrication, and characterization of our broadband modulator is presented in this work.

OCIS codes: (130.3120) Integrated optics devices; (160.3730) Lithium niobate; (230.4110) Modulators; (230.4000) Microstructure fabrication.

References and links

1. M. De Micheli, J. Botineau, P. Sibillot, D. B. Ostrowsky, and M. Papuchon, "Fabrication and characterization of titanium indiffused proton exchanged (TIPE) waveguides in lithium niobate," Opt. Commun. **42**(2), 101–103 (1982).
2. Y. Shi, "Micromachined wide-band lithium-niobate electrooptic Modulators," IEEE Trans. Microw. Theory Tech. **54**(2), 810–815 (2006).
3. M. Levy, R. M. Osgood, Jr., R. Liu, L. E. Cross, G. S. Cargill III, A. Kumar, and H. Bakhru, "Fabrication of single-crystal lithium niobate films by crystal ion slicing," Appl. Phys. Lett. **73**(16), 2293–2295 (1998).
4. G. Poberaj, H. Hu, W. Sohler, and P. Günter, "Lithium niobate on insulator (LNOI) for micro-photonic devices," Laser Photonics Rev. **6**(4), 488–503 (2012).
5. A. Rao and S. Fathpour, "Compact lithium niobate electrooptic modulators," IEEE J. Sel. Top. Quantum Electron. **24**(4), 1–14 (2018).
6. A. Guarino, G. Poberaj, D. Rezzonico, R. Degl'Innocenti, and P. Günter, "Electro–optically tunable microring resonators in lithium niobate," Nat. Photonics **1**(7), 407–410 (2007).
7. C. Wang, M. Zhang, B. Stern, M. Lipson, and M. Lončar, "Nanophotonic lithium niobate electro-optic modulators," Opt. Express **26**(2), 1547–1555 (2018).
8. V. Stenger, J. Toney, A. Pollick, J. Busch, J. Scholl, P. Pontius, and S. Sriram, "Integrated RF photonic devices based on crystal ion sliced lithium niobate," in L. P. Sadwick and C. M. O. Sullivan, eds. (2013), pp. 86240I 1–8.
9. A. J. Mercante, P. Yao, S. Shi, G. Schneider, J. Murakowski, and D. W. Prather, "110 GHz CMOS compatible thin film LiNbO3 modulator on silicon," Opt. Express **24**(14), 15590–15595 (2016).
10. L. Cai, Y. Kang, and H. Hu, "Electric-optical property of the proton exchanged phase modulator in single-crystal lithium niobate thin film," Opt. Express **24**(5), 4640–4647 (2016).
11. V. Stenger, J. Toney, A. Pollick, J. Busch, J. Scholl, P. Pontius, and S. Sriram, "Engineered thin film lithium niobate substrate for high gain-bandwidth electro-optic modulators," in *CLEO: Science and Innovations* (Optical Society of America, 2013).
12. L. Chen, J. Chen, J. Nagy, and R. M. Reano, "Highly linear ring modulator from hybrid silicon and lithium niobate," Opt. Express **23**(10), 13255–13264 (2015).

#328924 https://doi.org/10.1364/OE.26.014810
Journal © 2018 Received 20 Apr 2018; revised 21 May 2018; accepted 23 May 2018; published 25 May 2018

Optics EXPRESS

13. L. Chen, Q. Xu, M. G. Wood, and R. M. Reano, "Hybrid silicon and lithium niobate electro-optical ring modulator," Optica **1**(2), 112–118 (2014).
14. L. Chen, M. G. Wood, and R. M. Reano, "12.5 pm/V hybrid silicon and lithium niobate optical microring resonator with integrated electrodes," Opt. Express **21**(22), 27003–27010 (2013).
15. P. O. Weigel, M. Savanier, C. T. DeRose, A. T. Pomerene, A. L. Starbuck, A. L. Lentine, V. Stenger, and S. Mookherjea, "Lightwave circuits in lithium niobate through hybrid waveguides with silicon photonics," Sci. Rep. **6**(1), 22301 (2016).
16. A. Rao, A. Patil, P. Rabiei, A. Honardoost, R. DeSalvo, A. Paolella, and S. Fathpour, "High-performance and linear thin-film lithium niobate Mach-Zehnder modulators on silicon up to 50 GHz," Opt. Lett. **41**(24), 5700–5703 (2016).
17. P. O. Weigel, J. Zhao, K. Fang, H. Al-Rubaye, D. Trotter, and D. Hood, "Hybrid silicon photonic – lithium niobate electro-optic Mach-Zehnder modulator beyond 100 GHz," arXiv:1803.10365 (2018).
18. L. Chang, Y. Li, N. Volet, L. Wang, J. Peters, and J. E. Bowers, "Thin film wavelength converters for photonic integrated circuits," Optica **3**(5), 531–535 (2016).
19. L. Chang, M. H. P. Pfeiffer, N. Volet, M. Zervas, J. D. Peters, C. L. Manganelli, E. J. Stanton, Y. Li, T. J. Kippenberg, and J. E. Bowers, "Heterogeneous integration of lithium niobate and silicon nitride waveguides for wafer-scale photonic integrated circuits on silicon," Opt. Lett. **42**(4), 803–806 (2017).
20. Y. C. Shen, "Terahertz pulsed spectroscopy and imaging for pharmaceutical applications: A review," Int. J. Pharm. **417**(1-2), 48–60 (2011).
21. D. Shrekenhamer, C. M. Watts, and W. J. Padilla, "Terahertz single pixel imaging with an optically controlled dynamic spatial light modulator," Opt. Express **21**(10), 12507–12518 (2013).
22. M. C. Kemp, P. F. Taday, B. E. Cole, J. A. Cluff, A. J. Fitzgerald, and W. R. Tribe, "Security applications of terahertz technology," in R. J. Hwu and D. L. Woolard, eds. (2003), pp. 44–52.
23. T. Nagatsuma, G. Ducournau, and C. C. Renaud, "Advances in terahertz communications accelerated by photonics," Nat. Photonics **10**(6), 371–379 (2016).
24. J. Macario, P. Yao, S. Shi, A. Zablocki, C. Harrity, R. D. Martin, C. A. Schuetz, and D. W. Prather, "Full spectrum millimeter-wave modulation," Opt. Express **20**(21), 23623–23629 (2012).
25. K. Aoki, J. Kondou, O. Mitomi, and M. Minakata, "Velocity-matching conditions for ultrahigh-speed optical LiNbO3 modulators with traveling-wave electrode," Jpn. J. Appl. Phys. **45**(11), 8696–8698 (2006).
26. M. Lee, "Dielectric constant and loss tangent in LiNbO3 crystals from 90 to 147 GHz," Appl. Phys. Lett. **79**(9), 1342–1344 (2001).
27. D. K. Ghodgaonkar, V. V. Varadan, and V. K. Varadan, "A free-space method for measurement of dielectric constants and loss tangents at microwave frequencies," IEEE Trans. Instrum. Meas. **37**(3), 789–793 (1989).
28. D. L. K. Eng, B. C. Olbricht, S. Shi, and D. W. Prather, "Dielectric characterization of thin films using microstrip ring resonators," Microw. Opt. Technol. Lett. **57**(10), 2306–2310 (2015).
29. D. L. K. Eng, Z. Aranda, B. C. Olbricht, S. Shi, and D. W. Prather, "Heterogeneous packaging of organic electro-optic modulators with RF substrates," IEEE Photonics Technol. Lett. **28**(6), 613–616 (2016).
30. I. Krasnokutska, J. J. Tambasco, X. Li, and A. Peruzzo, "Ultra-low loss photonic circuits in lithium niobate on insulator," Opt. Express **26**(2), 897–904 (2018).
31. D. L. K. Eng, S. T. Kozacik, I. V. Kosilkin, J. P. Wilson, D. D. Ross, S. Shi, L. Dalton, B. C. Olbricht, and D. W. Prather, "Simple fabrication and processing of an all-polymer electrooptic modulator," IEEE J. Sel. Top. Quantum Electron. **19**(6), 190–195 (2013).
32. Y. Shi, L. Yan, and A. E. Willner, "High-speed electrooptic modulator characterization using optical spectrum analysis," J. Lightwave Technol. **21**(10), 2358–2367 (2003).
33. C. J. Huang, C. A. Schuetz, R. Shireen, S. Shi, and D. W. Prather, "LiNbO 3 optical modulator for MMW sensing and imaging," in R. Appleby and D. A. Wikner, eds. (2007), pp. 65480I–1–9.
34. M. Y. Frankel, S. Gupta, J. A. Valdmanis, and G. A. Mourou, "Terahertz attenuation and dispersion characteristics of coplanar transmission lines," IEEE Trans. Microw. Theory Tech. **39**(6), 910–916 (1991).
35. J. Chiles, M. Malinowski, A. Rao, S. Novak, K. Richardson, and S. Fathpour, "Low-loss, submicron chalcogenide integrated photonics with chlorine plasma etching," Appl. Phys. Lett. **106**, 111110 (2015).

1. Introduction

Despite its ubiquity in fiber-optic telecommunications and attractive nonlinear properties, the evolution of $LiNbO_3$ integrated optics can be considered sluggish relative to its Si and III-V counterparts. Discrete devices fabricated in bulk single crystalline $LiNbO_3$ generally rely on low index contrast optical waveguides with large bend radii [1], and specialized micromachining processes for sustaining broadband operation [2], which inhibits dense integration. Although the first instance of CIS $LiNbO_3$ was reported in 1998 [3], the recent widespread availability of full 75 mm wafers of CIS thin film $LiNbO_3$ from a number of distributors: NanoLN (China), Partow Industries (Florida), and SRICO (Ohio), has provided a fertile environment for $LiNbO_3$ device research and innovation [4,5].

Optics EXPRESS

Notable devices that take advantage of the high index contrast provided by a thin $LiNbO_3$ substrate are tunable ring resonators [6], Mach-Zehnder interferometers [7], switches [8], and standalone phase modulators [7,9–11]. Developed in parallel to these are various hybrid devices, that rely on either Si [12–17] or Si_3N_4 [16,18,19] for loading and guiding of an optical mode. A common theme among all devices mentioned herein is that they possess a reduced mode size. The reduced mode size leads to vastly improved EO activity over their bulk predecessors, most notably resulting in reduced half-wave voltages. Reduced half-wave voltage length products coupled with the ability to bend and fold the high index contrast optical waveguides leads to a substantially decreased device footprint ideal for future integrated photonic systems.

Up to this point however, the other major advantage of thin-film $LiNbO_3$, the significantly lower permittivity of the material system, has yet to be convincingly exploited [7,8,11,16]. To this end we present the first $LiNbO_3$-based EO modulator that is engineered to perform continuously from DC to THz frequencies. It is a device that can be used to optically up-convert RF signals directly at a system's RF front-end sensor, or antenna element. In so doing, the received RF signal becomes a sideband on an optical carrier that can be subsequently processed and, or routed using low loss conventional off-the-shelf optical components. A broad range of applications in the THz regime, including sensing [20], imaging [21,22], and high data rate communications [23], are currently limited by the inherent difficulties in routing THz signals electronically. Given the results presented in this work, we propose that optical routing of THz signals can be enabled by an EO up-converting modulator to provide both a simple and effective frontend alternative.

2. Device design and fabrication

A schematic of the broadband phase modulator's interaction region can be seen in Fig. 1(c), where the devices begin with commercially available CIS thin film $LiNbO_3$ on insulator procured from NanoLN. The substrate consists of a 700 nm thick *x*-cut $LiNbO_3$ device layer, affixed to a 500 µm thick quartz handle wafer via a 2 µm thick plasma enhanced chemical vapor deposited SiO_2 intermediate bonding layer. A single mode rib waveguide sustains the *y*-propagating TE polarized light to be modulated. The rib is 1.1 µm wide at the top and 1.8 µm wide at its base; the etch depth is 160 nm resulting in a sidewall angle of 24.57 degrees. Lumerical FDTD Mode Solver is used to simulate the waveguide structure and provides an effective optical group index (n_{opt}) of 2.2608 for the fundamental TE mode at 1550 nm. The discrepancy between bulk $LiNbO_3$'s optical indices ($n_{extraordinary}$ = 2.14 and $n_{ordinary}$ = 2.21) at a wavelength of 1550 nm and the simulated group index stems from structure dependent waveguide dispersion and $LiNbO_3$ material dispersion.

To form the optical waveguide an 80 nm thick chromium blanket layer is first sputtered onto the substrate. A soft-mask is patterned on top of the Cr layer with NR9-1500P photoresist from Futurrex. The soft-mask pattern is transferred into the Cr hard-mask with a time multiplexed Cl based inductively coupled plasma (ICP) dry etch. After pattern transfer, any residual resist is removed in an O_2 plasma ash. The waveguide pattern is finally transferred into the $LiNbO_3$ with a directional, highly anisotropic $LiNbO_3$ etch, obtained using an ICP CF_4 (6 sccm)/N_2 (28 sccm)/O_2 (0.5 sccm) etch. The etch is time multiplexed to prevent overheating of the sample. The number of cycles determines etch depth and each cycle consists of 1 minute etching in a 600 W plasma under 400 W bias. The etch rate of *x*-cut $LiNbO_3$ is ~27 nm per minute and the selectivity between $LiNbO_3$ and Cr is ~5.4:1. Any remaining Cr is stripped in a chemically selective wet etch.

Optics EXPRESS

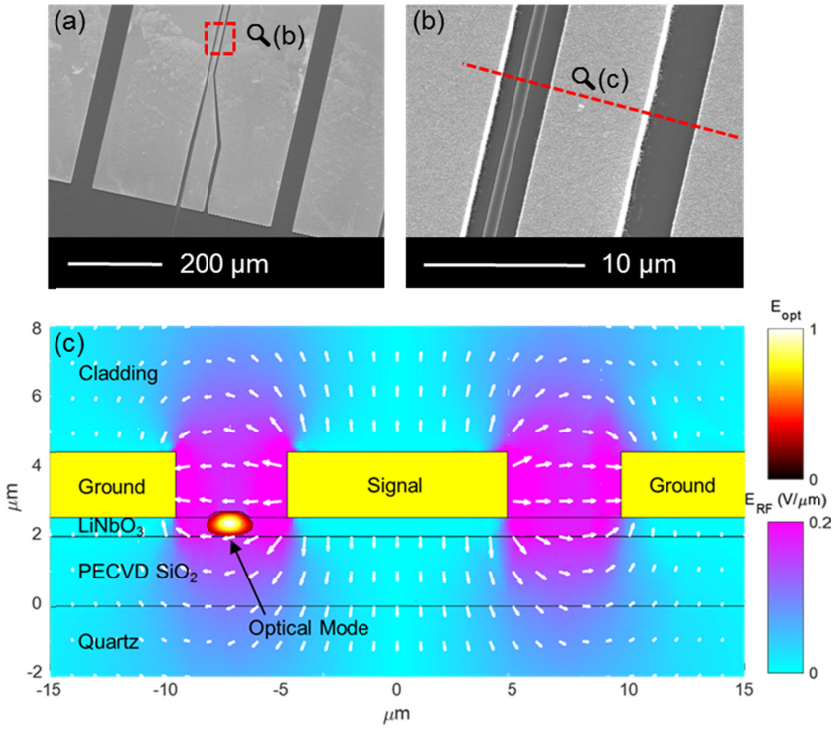

Fig. 1. (a,b) SEM images of a fabricated device's air-clad launch and interaction regions. (c) Cross-sectional schematic of the modulator's interaction region. Simulated results for both a modulating RF electric field at 110 GHz and a guided optical carrier possessing a wavelength of 1550 nm are overlaid onto the illustration. Data for the optical mode simulation is normalized to its maximum value, while the simulated RF field assumes that 1 V is applied across the GSG electrodes.

The modulating electric field is applied via electrodes in a CPW ground-signal-ground configuration, which are defined directly on top of the CIS $LiNbO_3$ device layer using a standard gold electroplating process and is accomplished in 4 steps: seed layer deposition, photolithography, electroplating, and seed layer stripping. First a Ti:Au:Ti seed layer is deposited via electron beam evaporation; thickness of each individual layer is 100 nm resulting in 300 nm total thickness. Next, photolithographic definition of the electrodes is done with NR9-3000P photoresist from Futurrex. After photoresist development, the resist is hard-baked at 120 ℃ for 30 minutes to drive off excess solvent so that the resist is able to survive the electroplating bath. Between lithography and electroplating, an O_2 plasma descum followed by a brief Ti wet etch in a hydrofluoric acid solution exposes the concealed Au seed layer. Au is then built up to the desired electrode thickness in an electroplating bath. Finally, photoresist and metal seed layers are stripped via iterated dips in $H_2SO_4(3):H_2O_2(1)$ solution, deionized water, and a KI based Au etchant. This cumulative process results in broadband CPW electrodes patterned directly on the $LiNbO_3$ surface. Figure 1 shows the fabricated optical waveguide situated in the gap between the signal and one of the ground pads of the CPW. Electrode dimensions in the modulator's interaction region for the thickness, signal width, and gap, are 1.8 μm, 9.5 μm, and 5 μm, respectively. The length of the fabricated interaction region is 0.92 cm and the simulated characteristic impedance of this structure is ~30 Ω up to 500 GHz. At the input and output of the device are 150 μm long probe pads that taper into the interaction region over another 150 μm length. The launch region probe pads possess a signal width of 53 μm and gap of 10 μm, the simulated characteristic impedance of the launch is ~50 Ω up to 500 GHz to match the impedance of the input probe. The 150 μm

Optics EXPRESS

long taper acts as an impedance transformer at both ends of the coplanar waveguide, achieving a conversion from 50 Ω launch to 30 Ω interaction region.

The primary concern with electrode design for a high-speed modulator's interaction region is matching the effective RF phase index of the CPW's guided mode (n_{RF}) with the optical waveguide's group index [24,25]. This is difficult to accomplish in bulk $LiNbO_3$ modulators as the RF index of $LiNbO_3$, roughly 6.55 at microwave frequencies [26], is significantly higher than the 2.14 extraordinary optical index at a wavelength of 1550 nm. Typically a combination of waveguide etching, addition of buffer layers, and thick electroplating are used to pull the modulating field from the bulk material and lower n_{RF} [24]. This strategy of removing the modulating field from the EO material can result in wideband modulator operation [24], but is at odds with achieving a low half-wave voltage, or V_π. In contrast, CPW design for thin film $LiNbO_3$ modulators requires the opposite approach compared to velocity matching in a bulk device. Low permittivity quartz possessing an RF index as low as 1.95 [27], makes up the majority of the thin film device, resulting in a naturally lower n_{RF}. Simulated n_{RF} values are extracted from Ansys HFSS models of the aforementioned device and are shown in Fig. 2, where at 110 GHz the simulated n_{RF} is equal to 2.02. The disparity between simulated n_{RF} and n_{opt} is ~0.24, and if fabricated, this device will have a reduced operational bandwidth due to this index mismatch. Within the literature, a proven method for increasing n_{RF} is cladding the modulator's interaction region in a higher index material, such as UV15 adhesive possessing an RF index near 1.73 [28,29]. Accordingly, a 20 μm thick cladding is applied to the interaction region of our device. By adding a UV15 cladding layer to the HFSS model, the simulated n_{RF} at 110 GHz increases from 2.02 to 2.26. The cladding's impact on the simulated optical group index according to simulations is a slight decrease from 2.26 to 2.24, which also helps to match modal indices overall. The UV15 tuning layer is applied via brush to the device's interaction region. Flood exposure from a UV light source sets the epoxy in place. As a final step in the fabrication process, single mode fiber V-grooves are aligned and bonded to the end facets of the device with a UV curable adhesive in preparation for testing on a probe station.

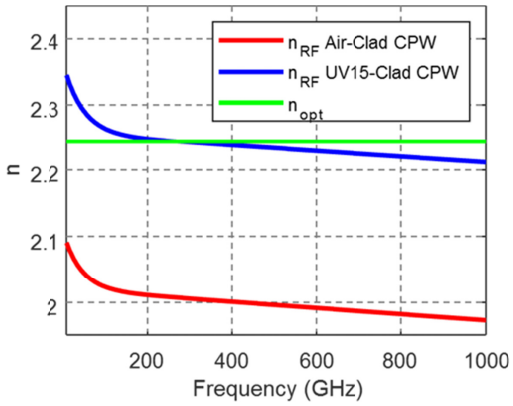

Fig. 2. Simulated effective indices, three traces are plotted. The red and blue traces represent the simulated RF effective phase indices of a device under two different cladding circumstances. The green trace is the simulated optical group index of a UV15 cladded optical waveguide at an optical wavelength of 1550 nm.

3. Experimental setup and characterization

Optical waveguide propagation loss of ~7 dB/cm is measured via the cutback method. This result is comparable to propagation losses seen elsewhere in literature for dry etched thin film $LiNbO_3$ ridge waveguides [4], although through refined processing techniques similar devices have demonstrated propagation losses as low as 0.4 dB/cm [30]. The total optical loss of the

Optics EXPRESS

characterized 1.5 cm long modulator is ~40 dB, 10.5 dB of which can be attributed to the propagation loss. Remaining insertion loss is accounted for by the modal mismatch between the single-mode optical fibers and ridge etched $LiNbO_3$ waveguides. The spot size of the fibers possesses a Gaussian profile with an 8 μm waist and the asymmetric spot size of the rib waveguide according to FDTD simulation is ~2 μm laterally by ~0.7 μm vertically. While not the focus of this work, proper design of the coupling structure can significantly reduce loss.

The DC-V_π, scattering parameters, and optical sideband measurements are used to characterize this device. The DC-V_π is measured to be 3.8 V by means of a polarization rotation method [31], which is in agreement with our simulated DC-V_π of 3.4 V. Two port scattering parameters are collected up to 110 GHz using an Agilent E8316C Programmable Network Analyzer (PNA), in conjunction with two Agilent N5260 T/R modules, and two 1 mm cable-fed GGB Industries Inc. probes in GSG configuration. The same PNA setup is used to apply the modulating RF signal up to 70 GHz. An Agilent E4418-B power meter measures the RF power output which is delivered to the probe in this range, measured power output is later used for normalization. Above 70 GHz the measurements are conducted in five different frequency ranges, 70-115 GHz, 115-140 GHz, 140-220 GHz, 220-325 GHz and 325-500 GHz. Each additional band corresponds with a VNA extension module from Virginia Diodes Inc. An assortment of waveguide-fed probes from GGB industries and Dominion MicroProbes probes are used to apply the modulating signal in these bands. Above 70 GHz an Erickson PM4 power meter determines the RF power available to the probe's waveguide input. The device's modulated optical output is fed directly into a Yokogawa AQ6319 Optical Spectrum Analyzer (OSA) and the strength of the modulation sidebands are observed [32]. The optical power fed to the modulator input is a constant 20 dBm at 1550 nm. The lowest RF input power occurs at a modulation frequency of 350 GHz and is −24 dBm, this value includes probe insertion loss.

Using this setup optical sidebands up to 500 GHz are measured. In Fig. 3 the sidebands are plotted at 5 GHz increments. For clarity only upper sidebands are shown in the figure, but each set of sidebands corresponds to the modulator's electro-optic response normalized to the measured input power at the corresponding modulating frequency. Probe insertion loss, feed loss, and harmonic generation in the modulating signal source are all accounted for in the optical sideband normalization. The index matched modulator shows a frequency response up to the measured 500 GHz with a roll off of 19 dB from DC. Simulated effective indices suggest that at 1 THz the modal index mismatch is 0.03 and based on this we predict that the EO response of this device will extend to 1 THz with a total roll off of 29 dB from DC. However, characterization of our device is limited to 500 GHz by available equipment.

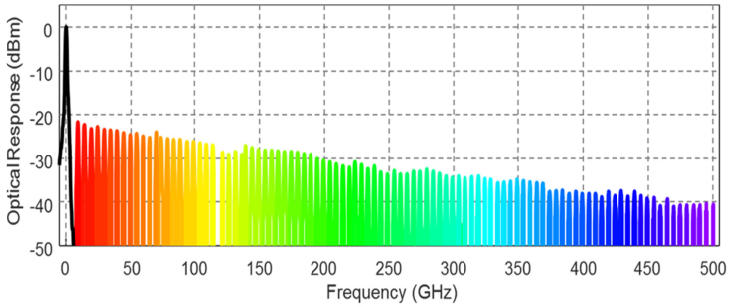

Fig. 3. Normalized optical modulation spectra of a 1550 nm optical carrier modulated up to 500 GHz. This is a symmetric spectrum but for clarity only the upper portion is displayed.

Plotted in Fig. 4(a) are half-wave voltages shown as a function of frequency. Measured values for half-wave voltage are extracted from the sideband data shown in Fig. 3 through the following relation, $V_\pi(f) = \pi\sqrt{Z_{in}(f)/(2P_{sb}(f))}$ [33] where $Z_{in}(f)$ is the CPW characteristic

Optics EXPRESS

impedance and $P_{sb}(f)$ is the power in Watts of the normalized optical sideband. The calculated V_π trace is based on our simulated DC-V_π value, simulated effective indices, and the CPW scattering parameters. The S_{21} transmission parameter used for V_π calculation is measured up to 110 GHz, shown in Fig. 4(b), and then extrapolated to 500 GHz. The extrapolation of S_{21} accounts for radiative losses which are expected to become prevalent beyond 200 GHz [34].

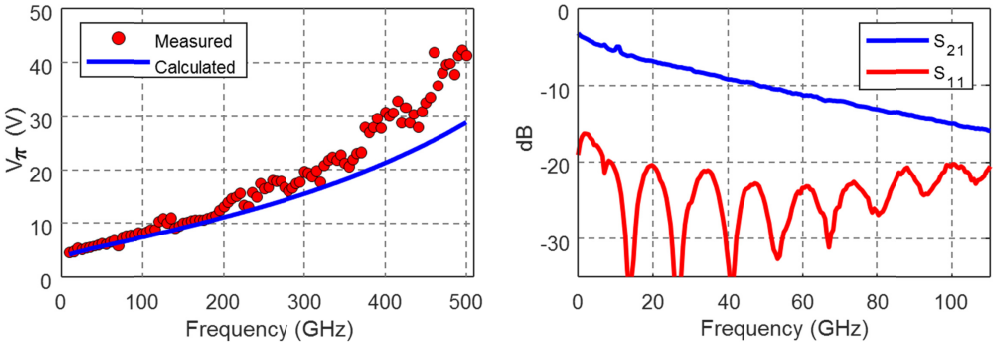

Fig. 4. (a) Measured and calculated modulator half-wave voltages are presented. The measured trace is extracted from the sideband measurements. The calculated trace is based on the simulated DC-V_π, the measured/extrapolated S_{21} transmission parameter, and the simulated effective indices. (b) Measured transmission S_{21} and reflection S_{11} parameters of a fabricated device's CPW electrodes.

4. Conclusion

Presented in this paper is, to the best of our knowledge, the first instance of an index-matched travelling wave CIS $LiNbO_3$ modulator having a measured frequency response up to 500 GHz. The modulator's unparalleled electro-optic performance makes it an ideal candidate for emerging technologies in the THz regime, including sensing [20], imaging [21,22], and high-data-rate communications [23]. Future work will require investigation of methods for efficiently coupling light into and out of the device, whether it be within the context of hybrid integration [12,13,15,17,19] or standalone use [7,9,24,35], as well as minimizing CPW THz radiation losses.

Funding

Air Force Office of Scientific Research (FA9550-14-1-0198).

Acknowledgments

The authors gratefully acknowledge the support of Dr. Robert Nelson, and Dr. Attila Szep from the U.S. Air Force Research Laboratory as well as Dr. Gernot Pomrenke from the Air Force Office of Scientific Research, among other U.S. Government agencies.